Cellular harmonics for the morphology-invariant analysis of molecular organization at the cell surface

Hanieh Mazloom-Farsibaf[1,2], Qiongjing Zou [1], Rebecca Hsieh[1], Gaudenz Danuser [1,2] ✉ & Meghan K. Driscoll [1,2,3] ✉

The spatiotemporal organization of membrane-associated molecules is central to the regulation of cellular signals. Powerful new microscopy techniques enable the three-dimensional visualization of localization and activation of these molecules; however, the quantitative interpretation and comparison of molecular organization on the three-dimensional cell surface remains challenging because cells themselves vary greatly in morphology. Here we introduce u-signal3D, a framework to assess the spatial scales of molecular organization at the cell surface in a cell-morphology-invariant manner. We validated the framework by analyzing synthetic signaling patterns painted onto observed cell morphologies, as well as measured distributions of cytoskeletal and signaling molecules. To demonstrate the framework's versatility, we further compared the spatial organization of cell surface signals both within, and between, cell populations, and powered an upstream machine-learning-based analysis of signaling motifs.

Many cell functions depend on the subcellular regulation of signal transduction. Cells regulate signaling patterns through nonlinear circuitry of activators and inhibitors, and by directly controlling the localization of molecular components[1,2]. Confinement on membranes, in scaffolds, or via phase separation, all serve to localize reactions[3]. Accordingly, molecular activities vary across space and time, requiring live cell microscopy and appropriate image analytics for quantifying cell signaling.

One of the most important organizers of molecular signals is the plasma membrane itself[4]. The plasma membrane acts as both a platform and a conduit for the chemical reactions that range from local nano- or microscale puncta to global bursts that span the entire cell (Fig. 1a)[5,6]. Deciphering the regulatory principles that define these scales requires a comprehensive quantification of molecular concentration and activity at the three-dimensional (3D) cell membrane. This task is complicated by the fact that cells configure their plasma membranes into a wide range of 3D morphologies[7]. Signaling data, such

as those probed by a fluorescence biosensor of protein activity, can be projected onto the 3D cell surface to facilitate analysis (Fig. 1b)[7–9]. However, this alone does not enable quantitative comparisons of signaling organization. A natural ordering or parameterization of the surface signal is required that is consistent across variable morphologies.

To normalize surface signal distributions, 3D analysis frameworks have considered a combination of geometric and molecular organization[10], constrained cell shape by micropatterned surfaces[11] or normalized the cell shape on the basis of global cell shape features[12–14]. Tools to normalize and analyze molecular distributions in cells adopting unconstrained morphologies are missing.

We propose a spectral approach, in which the surface distribution is broken down into a set of elementary modes that spans a wide range of spatial scales. A natural candidate for spectral decomposition of data on the cell surface is the Laplace–Beltrami operator (LBO), which constructs a mathematically complete set of Fourier-like modes on surfaces[15,16]. These modes are invariant to isometric transformations[17]

[1]Lyda Hill Department of Bioinformatics, University of Texas Southwestern Medical Center, Dallas, TX, USA. [2]Cecil H. & Ida Green Center for System Biology, University of Texas Southwestern Medical Center, Dallas, TX, USA. [3]Present address: Department of Pharmacology, University of Minnesota, Minneapolis, MN, USA. ✉e-mail: Gaudenz.Danuser@utsouthwestern.edu; drisc269@umn.edu
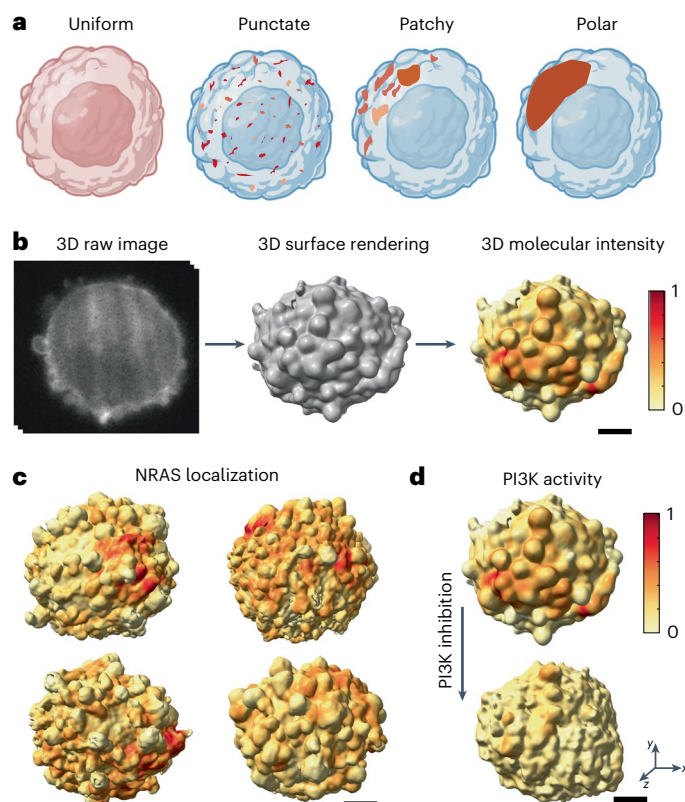
Fig. 1 | Spatial organization of molecular distributions on the 3D cell surface. a, Membrane-associated proteins (brown) can spatially organize across scales ranging from a uniform distribution or punctate clustering to a highly polarized configuration. **b**, Three-dimensional raw image of an MV3 melanoma cell with phosphoinositide 3-kinase (PI3K) activity labeled using a fluorescent biosensor (GFP-AktPH) (left), surface rendering of the same cell (middle), with localization of PI3K activity projected onto the 3D cell surface (right). Red surface regions indicate high local PI3K activity. **c**, NRAS-GFP (Green Fluorescent Protein-tagged version of the GTPase NRas) localization projected onto the 3D cell surface of MV3 melanoma cells. **d**, PI3K activity projected onto an MV3 melanoma cell before (top) and after (bottom) treatment with a PI3K inhibitor. Scale bars, 2 μm.

and are independent of shape representation, parametrization and spatial position. These properties have been leveraged in computer science to quantify the global characteristics of 3D shapes[17,18], and the LBO has been modified to represent local morphological motifs[19–22]. Due to its ubiquitous use in the computer graphics field, the efficiency and stability of LBO implementations have been extensively characterized[23–25]. In the biomedical sciences, the LBO has been used to describe brain images[26–30], and spherical harmonics—the LBO modes of a sphere—have been used to represent 3D cell shapes[31–33]. Here we exploit the LBO to establish a spectral representation of the cell surface signal variation that is agnostic to the underlying cell shape variation. Specifically, we introduce u-signal3D, a cellular manifold harmonics pipeline to: (1) compare the spatial organization of signaling over time (Supplementary Video 1) or across cell populations (Fig. 1c); (2) measure subcellular signaling responses to acute experimental intervention (Fig. 1d); (3) perform generative modeling of representative signaling distributions; and (4) classify features of signaling distributions across cells and conditions via machine learning.

Results

Pipeline overview
The u-signal3D pipeline accepts 3D images or triangle meshes with associated signaling data as inputs, and outputs spectra describing the spatial organization of surface signal distributions that can be compared across morphologies. For convenience, the pipeline includes the cell surface segmentation functionality of our previous software pipeline, u-shape3D, which generates surface meshes from 3D images[34]. To meet the numerical requirements for LBO applications, we modified u-shape3D's mesh-generating process to keep only a single mesh component (Supplementary Fig. 1a and Methods). The u-signal3D pipeline incorporates two implementations of the LBO: one optimized for computational speed[35,36] and another that is robust on non-manifold meshes[24] (Supplementary Fig. 1b and Methods).

The LBO computes the local geometrical variation of a 3D surface and defines a mathematically complete set of manifold harmonic functions we called cellular harmonics; these are ordered by increasing frequency and conform to the morphology of the structure (Fig. 2a). The cellular harmonics simultaneously encode the spatial scale and orientation relative to the cell shape. For an irregularly shaped cell, the morphological complexity complicates intuitive interpretations of these harmonics. In the limit of a perfect sphere, the LBO yields the hierarchy of the spherical harmonics, with functions at low frequency levels capturing surface signal variations that span the entire sphere, as well as functions at higher levels capturing increasingly finer-grained variations (Fig. 2b and Methods). In general, the LBO yields manifold harmonics similar to spherical harmonics, but conformed to the geometrical undulations of particular 3D morphologies. We therefore arranged the LBO modes into a spherical harmonics-style pyramid (Fig. 2ci). Mathematically, the eigenvectors of the LBO form an orthogonal basis of R^N, where N is the number of mesh vertices. Hence, the eigenvalues can be considered pseudo-frequencies of the geometry defined over the mesh graph and ordered inversely with the length scale of surface undulation (Fig. 2cii). Surface-associated molecular distributions can therefore be quantified by projection of the pattern onto the LBO eigenvectors.

Characterizing molecular distributions on the cell surface
We demonstrate the spectral representation of cellular signals by the LBO for a fluorescent reporter of phosphoinositide 3-kinase (PI3K) activity on the surface of MV3 melanoma cell (Fig. 2di). The contribution of each eigenvector to the total surface signal is visualized via the function pyramid of Fig. 2ci weighted by the magnitude of the matching eigenprojection (Supplementary Fig. 2a). PI3K activity has previously been shown to follow a polarized distribution with increased signaling at the cell front[37]. Accordingly, the strongest eigenprojections associate with eigenvectors at level $L = 1$ (black arrow, Fig. 2dii), whereas the projections for higher levels decrease near monotonically.

Distinct cell states are associated with distinct signaling patterns, encoded by contributions from different spatial scales; however, the pattern orientation, determined by the relative weights of the basis functions at one scale, can be ignored. Thus, to calculate an interpretable spectral signature for any given cell surface pattern, we separated spatial frequency from pseudo-orientation by integrating across the spherical harmonics levels.

The overall intensity of the fluorescence signal often varies between cells due to the concentration of the probes. To eliminate this factor, we first normalized the fluorescence intensity and further calculated an energy density across levels. This energy measures the signal gradient under Dirichlet boundary conditions, which is valid for a closed 3D shape (see Methods). The Dirichlet energy density provides a quantitative measure of how much each frequency level contributes to the organization of the surface signal. For the PI3K activity in Fig. 2di, the Dirichlet energy density reveals that the signal is organized across a range of higher spatial frequencies beyond the low-level frequencies that capture front–back polarization (black arrow, Fig. 2diii).

Given the parameterization of a surface signaling pattern by frequency levels, we can regenerate subpatterns containing only particular spatial scales. For example, we reconstructed the PI3K
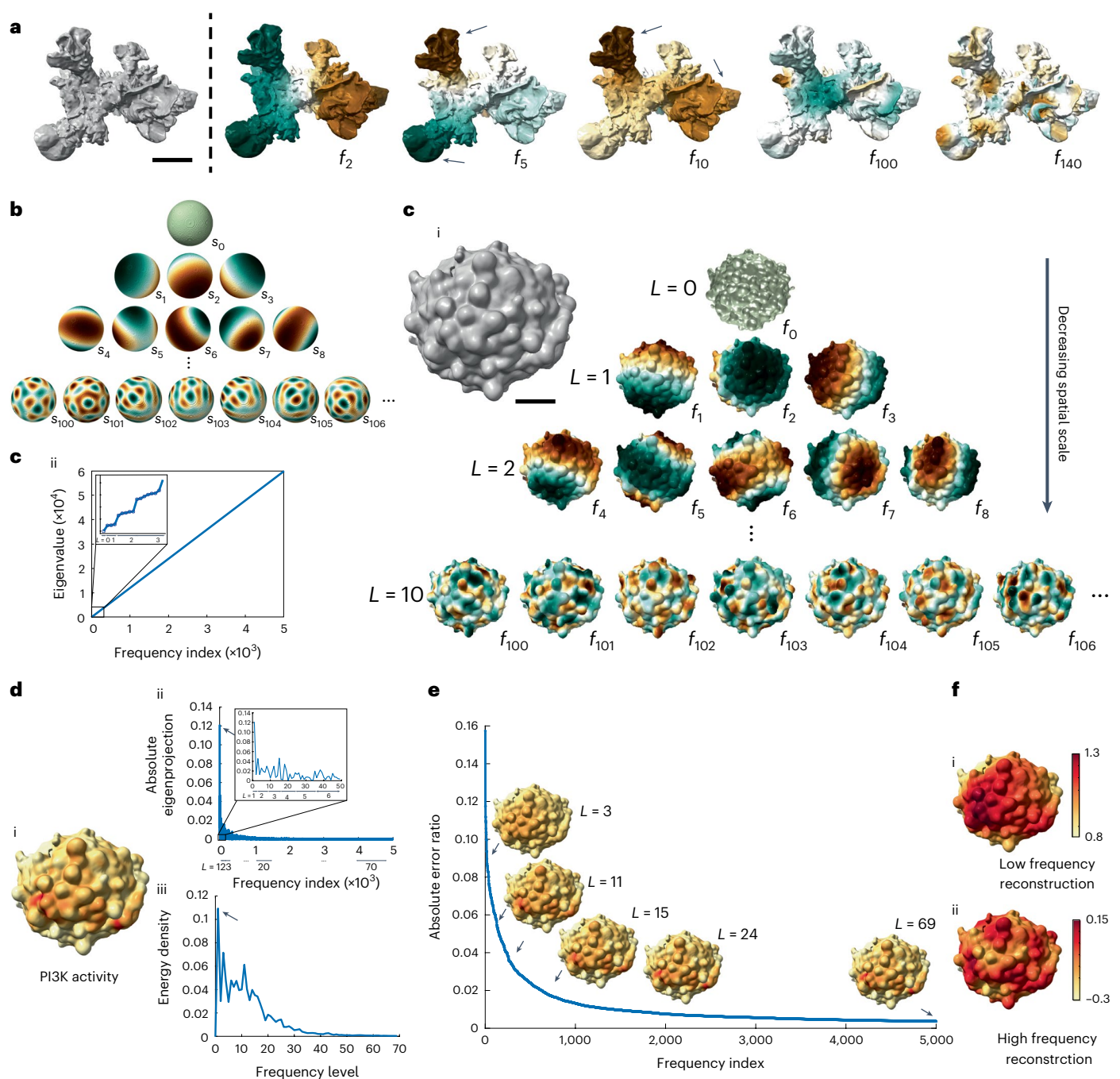
Fig. 2 | Cellular harmonics for the analysis of molecular distributions on the 3D cell surface. a, Surface rendering of a dendritic cell (left) and select modes of its cellular harmonic basis (f_i) (right). Brown and green colors represent positive and negative values, respectively. Black arrows indicate eigenvector magnitudes that follow protrusions in the underlying cell morphology. The cell surface was generated from the Lifeact-GFP-signal visualizing cortical actin filament structures (data not shown). Scale bar, 2 μm. **b**, Select modes of the spherical harmonic basis (s_i), representing LBO eigenvectors applied to a sphere. The spherical harmonics naturally organize into a pyramid. **ci**, Top left: surface rendering of an MV3 melanoma cell expressing GFP-AktPH, a marker of PI3K activity. Scale bar, 2 μm. Bottom right: LBO eigenvectors (f_i) arranged hierarchically into a pyramid from low to high frequency levels (L_j). **cii**, LBO

eigenvalues plotted as a function of LBO frequency index. The inset is a magnified region of the LBO eigenvalues plot showing only the first three frequency levels. **d**, Surface signal parameterization using cellular harmonics. **di**, PI3K activity projected onto the cell surface shown in **c**. **dii**, Absolute value of the LBO eigenprojection profile over the cellular harmonics index. **diii**, Energy density spectra of PI3K activity over frequency levels. **e**, Absolute error ratio between the reconstructed data and the original signal as a function of the number of frequency indices in the reconstruction. Black arrows indicate 3D reconstructed data visualized up to levels, $L = 3, 11, 15, 24$ and 69. **f**, Reconstructed PI3K activity from the LBO eigenvectors showing only low- ($L = 1$ to 20) or high-frequency ($L = 20$ to 69) information. Color scale is adjusted for visualizing the high-frequency variations.
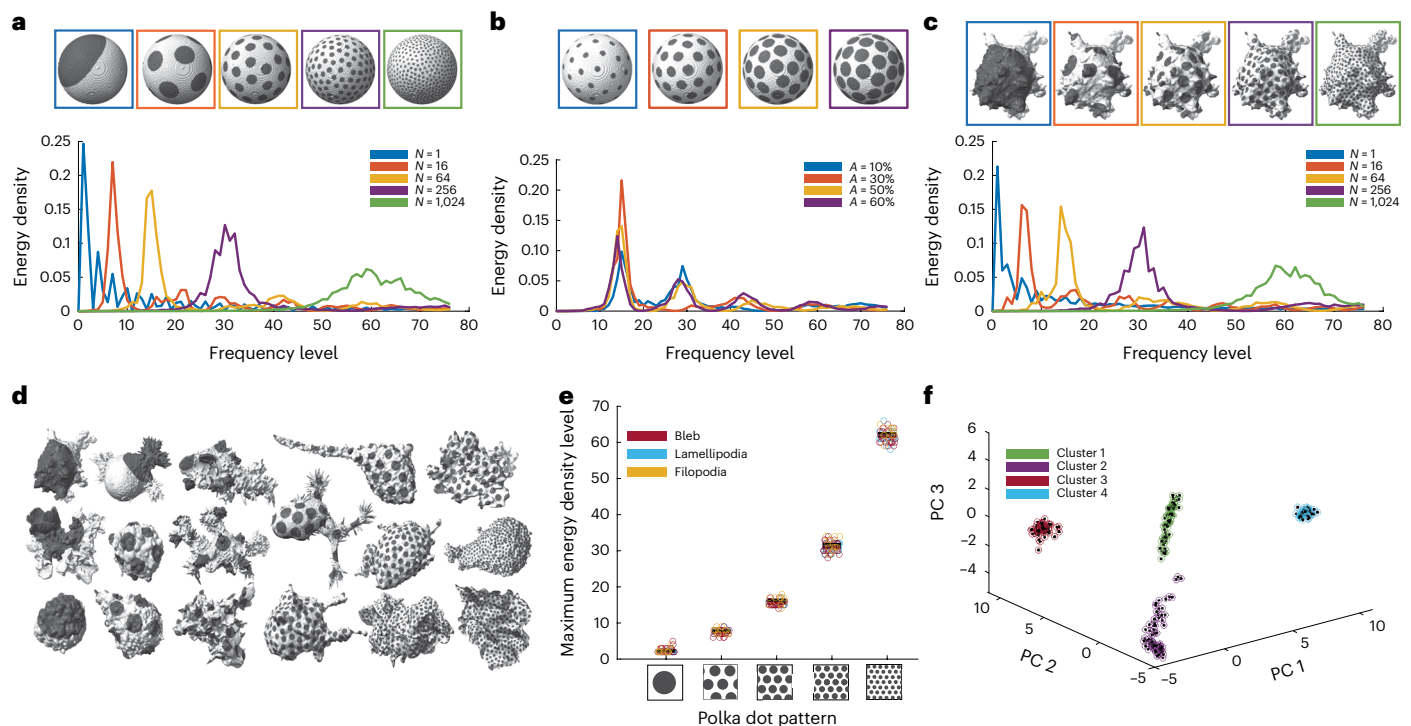
Fig. 3 | Validation and robustness of spectral decomposition analysis.
a, Polka dot patterns on a sphere with increasing numbers of dots, from left to right $N = 1, 16, 64, 256$ and $1,024$ (top), and corresponding energy density spectra (bottom). **b**, Polka dot patterns on a sphere with 64 dots painting 10%, 30%, 50% and 60% of the total surface area (top), and corresponding energy density spectra (bottom). **c**, Polka dot patterns as in **a** applied to the 3D cell surface of an MV3 melanoma cell expressing tractin-GFP (top), and corresponding energy density spectra (bottom). **d**, Polka dot patterns on a variety of MV3 melanoma cells, dendritic cells and human bronchial epithelial cells (HBECs). Numbers of dots number increase from left to right $N = 1, 16, 64, 256$ and $1,024$. **e**, Scatter plot of the energy density peak for 67 MV3 (morphological motif is blebs), dendritic (morphological motif is lamellipodia) and human bronchial epithelial (morphological motif is filopodia) cells painted with polka dot patterns of $N = 1, 16, 64, 256$ and $1,024$ dots. **f**, Principal component (PC) analysis of energy density spectra for the cells in **e** with polka dot patterns of $N = 16, 64, 256$ and $1,024$ dots. Colored circles are clusters determined via the k-means algorithm.

activity using LBO eigenvectors up to $L = 3, 11, 15, 24$ and 69 (Fig. 2e). The absolute error ratio between reconstructed and original signal decreases with inclusion of higher frequency levels (Fig. 2e and Supplementary Fig. 2b), confirming that LBO eigenvectors describe the signal completely given sufficient eigenvectors. This property can be leveraged for denoising the signaling patterns by suppression of high-frequency basis functions (Supplementary Fig. 2c). Moreover, we were able to separate low- from high-frequency components, with the former representing the signaling pattern at the cell scale, and the latter the spatial distribution of localized signaling hotspots (Fig. 2f).

Validation of spectral decomposition on the cell surface
To validate the decomposition of cell surface signals across spatial scales, we generated synthetic patterns on both experimental and modeled cell geometries. The frequency-dependent behavior of optical instruments is commonly assessed via stripe patterns such as Ronchi rulings[38]. Stripe patterns cannot be applied to the highly curved surfaces of cells with any consistency. We instead introduced polka dots consisting of circular shapes of equal radius, arranged as far apart as possible on the cell surface (Supplementary Fig. 3a and Methods). Generating variously scaled polka dot patterns allowed us to simulate surface signal distributions ranging from front–back polarization to punctate microclusters (Fig. 3a). Applied to a sphere, coarse-to-fine-grained polka dot patterns yielded spectral peaks at increasingly higher frequency levels (Fig. 3a). For each pattern, secondary lower peaks occur due to sharp boundaries at the polka dot edge. They vanish upon smoothing the polka dot pattern (Supplementary Fig. 3b). The primary peaks across various patterns broaden at higher frequencies. Although the spherical harmonics have the same spatial angular frequency

at each pyramid level, the number of peaks varies (Supplementary Fig. 4a). At higher frequency levels, similar peak numbers are shared by a greater range of levels (Supplementary Fig. 4b). Consequently, polka dot number and angular spatial frequency are not perfect analogues, even though both capture spatial scale information. Furthermore, changing the dot radius changes the energy spectra peak magnitude without changing its corresponding frequency level (Fig. 3b and Supplementary Fig. 3c), demonstrating that the relative distance and number of dots determine the spatial scale of a pattern, not the dot radius.

Analyzing the same polka dot patterns on an MV3 melanoma cell surface, we recovered spectra similar to the patterns on the sphere (Fig. 3c). Hence, the spectral decomposition is largely independent of the underlying surface morphology. To more formally test the consistency of spectra across cell morphologies, we first applied a polka dot pattern to a sphere and similarly sized ellipsoids (Supplementary Fig. 3d). Regardless of shape eccentricity, the spectra coincided. We then applied five different patterns to a cell library with blebs (hemispherical membrane protrusions), lamellipodia (thin, sheet-like membrane protrusions), or filopodia (elongated and spiky membrane protrusions) (Fig. 3d and Supplementary Fig. 5)[34]. We found consistent spectral peaks over 67 different cell morphologies (Fig. 3e). Our spectral decomposition thus characterizes the spatial scales of cell surface patterns in a cell shape-agnostic manner.

To validate the conclusions from these synthetic data in more general scenarios, we first painted only a portion of the cell surface with polka dots to break the uniformity (Supplementary Fig. 6a). The energy spectra peak at the frequency level of the uniform pattern, but the asymmetry of surface coverage generates a second, weaker, low-frequency
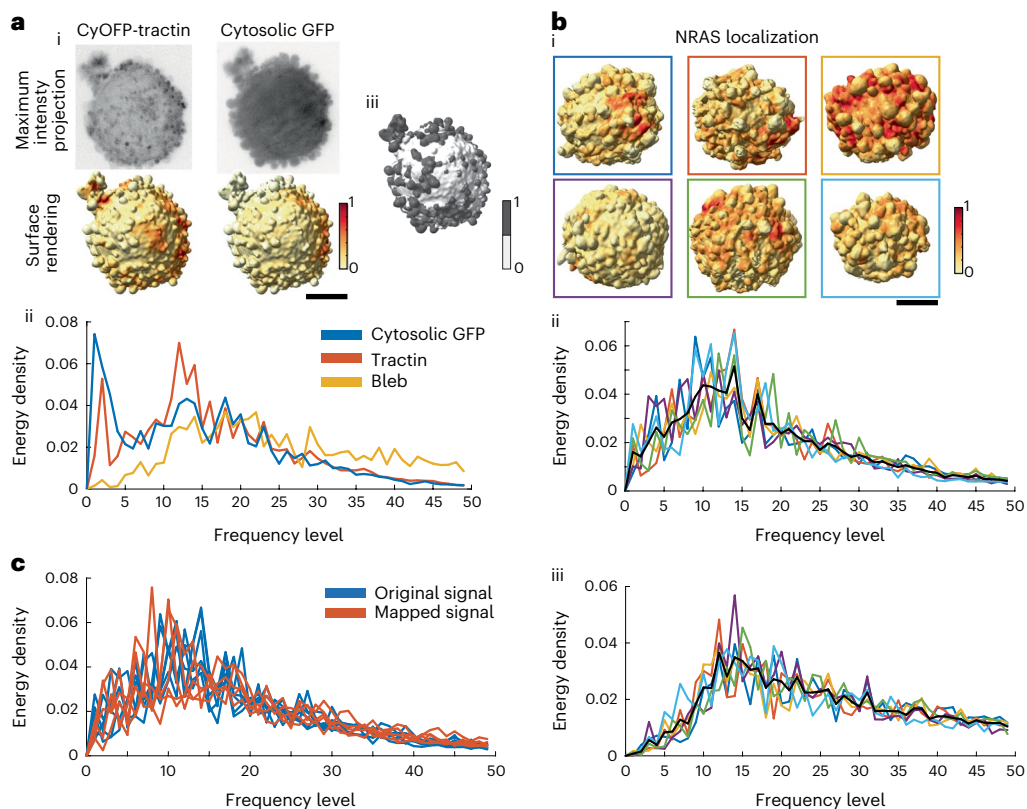
Fig. 4 | Decomposing the spatial organization of cell surface signaling on melanoma cells. ai, Top: maximum intensity projections of an MV3 melanoma cell labeled with an actin marker, CyOFP-tractin and cytosolic GFP. Bottom: surface renderings of the same cell with fluorescence intensities projected onto the surface. Red and yellow indicate regions of high and low fluorescence intensity, respectively. **aii**, Energy density spectra of a cytosolic marker, CyOFP-tractin and the binary on/off-bleb distribution. **aiii**, Segmentation of blebs (dark gray) versus non-bleb (white) was performed using u-shape3D software[34].

Scale bar, 2 μm. **bi**, Surface renderings of MV3 melanoma cells expressing NRAS-GFP with fluorescence intensities projected onto the cell surfaces. Scale bar, 2 μm. **bii,biii**, Energy density spectra of NRAS localization (**bii**) and bleb distribution (**biii**). Line colors in correspondence with box colors in **bi**. The black curve in each panel is the average energy density spectra across six cells. **c**, Energy density spectra of NRAS localization of MV3 melanoma cells ($n = 5$) on the original mesh, and mapped to a new mesh.

peak. We also confirmed that our framework could properly detect the superposition of two patterns with distinct dot numbers (Supplementary Fig. 6b). We subsequently distributed the polka dots randomly (Supplementary Fig. 6c). Compared with the energy spectra of uniform patterns, the corresponding non-uniform patterns generated spectra with similar dominant frequency levels but wider peaks. Hence, the peak frequency reflects the average distance between polka dots, even when individual neighbor-to-neighbor distances vary across the cell. Finally, we tested the sensitivity of the energy spectra to noise (Supplementary Fig. 7). We employed two methods to disturb a given baseline polka dot pattern: (1) we changed the intensity value of every surface mesh node by adding a random value from a uniform distribution (intensity noise); (2) we spatially blurred the pattern by translocating the value of a surface mesh node to another node in a predefined neighborhood (spatial shuffling). The energy spectrum of a surface signal with random intensity values in every mesh node increases monotonically across the frequency levels (Supplementary Fig. 7a), indicating the implicit low-pass filtering properties of the LBO. We added noise of increasing intensity to a polka dot pattern until the dominant pattern vanished (see Methods). Low-level noise marginally altered the measured spectra of polka dot patterns or molecular distributions. However, when the range of noise began to equal that of the signal, the effects of the noise dominated the spectra, regardless of the dot size, and particularly at high frequency levels (Supplementary Fig. 7b–e). The peaks of the energy spectra are remarkably resistant to spatial shuffling, in line with our previous conclusion that the spectrum maxima capture the mean

distance between the dots (Supplementary Fig. 7f). The energy spectra only increased at high frequency levels outside of the frequency band of the underlying pattern when the shuffling neighborhoods became similar to, and greater than, the dot size. Finally, we tested the sensitivity of the spectra to reduction in mesh density while maintaining the cell shape (Supplementary Fig. 8a). The energy spectra remain remarkably similar even with a 100-fold reduction in surface mesh nodes, although the maximum frequency level is limited to the number of vertices.

Measuring cellular harmonics further allows us to parameterize surface signals for downstream analyses such as machine learning applications. In Fig. 3f we show the application of principal component analysis to reduce the dimensionality of the energy density spectra on 67 cell morphologies of the four polka dot patterns introduced in Fig. 3d,e. Independent of the cell morphology, each polka dot pattern appears as a distinct cluster in the reduced space of the first three principal components. Performing a similar cluster analysis directly on the intensities projected onto the cell surface is impossible as there is no natural ordering of intensities that is consistent between cells with highly diverse morphologies.

In summary, our validation based on polka dots established the ability of the pipeline to measure the spatial organization of cell surface patterns independent of the underlying cell shape.

Spectral analysis of molecular patterns on cell surfaces

To illustrate the utility of cellular harmonics in biological experiments, we analyzed molecular distributions on melanoma cells imaged in

3D culture by high-resolution light-sheet microscopy[37,39,40]. First, we compared the cell surface distributions of two co-imaged molecular signals. Melanoma cells in soft collagen tend to extend dynamic blebs[39]. Expanding blebs are thought to be largely devoid of cortical actin, whereas retracting blebs have increased cortical actin[41]. Thus, a snapshot of cortical filamentous actin at a single time-point of a blebbing cell is expected to display a patchy fluorescent signal over the entire cell surface (Fig. 4ai and Supplementary Video 2). We measured the localization of filamentous actin (labelled by the cyan-excitable orange fluorescent protein tractin, abbreviated to CyOFP-tractin) and a cytosolic green fluorescent protein (GFP) marker within a 1 µm sampling radius of the cell surface. Averaged across five cells, filamentous actin shows peaks in spatial organization at mid-range energy levels with the maximum at $L = 13$ and a full-width at half-maximum (FWHM) of 15 levels (Fig. 4aii and Supplementary Fig. 8b). Surprisingly, the cytosolic marker also shows spatial organization across a range of energy levels with wider FWHM (20 levels), suggesting that its distribution is not homogenous. Indeed, the raw data (Supplementary Video 3) display a spatial patterning, including a reduction in intensity within blebs, probably due to the limited diffusion of GFP molecules into the narrow space of blebs. Of note, the first peak in both cytosol and tractin energy density spectra is associated with an illumination gradient across the entire cell, which is clearly recognizable in the maximum projection images (Fig. 4ai).

To enable interpretation of energy spectra, we calculated an approximate conversion between energy level and actual spatial scale by measuring the relative distances among polka dots distributed on 11 blebby cells (Supplementary Fig. 8c). Comparison between the spectra of CyOFP-tractin and polka dot patterns for MV3 cells suggests that filamentous actin is organized at a peak length scale of 7 µm for the energy peak at $L = 13$ (Supplementary Fig. 8c). Moreover, these analyses indicated that 50 frequency levels are sufficient to represent energy density spectra at spatial resolutions above 1 µm, which is the limit imposed by the sampling radius of the fluorescence intensity (see Methods and dashed line in Supplementary Fig. 8c). To test the possibility that the spatial pattern of actin filaments relates to the spatial pattern of blebs, we detected blebs using the u-shape3D software[34] and converted the segmentation into a binary cell surface pattern (Fig. 4aiii). The energy spectra of bleb distribution peaks ($L = 16$ with a FWHM of 17 levels) at a spatial scale of 5 µm (Supplementary Fig. 8c), that is, at somewhat higher frequency ranges than the CyOFP-tractin signal. Hence, on a blebby cell, the filamentous actin density varies over longer distances than bleb formation, as one would expect for a snapshot, in which only the fraction of retracting blebs is filled with actin filaments.

We next analyzed the spatial organization of wild type GTPase NRas (NRAS) signaling in melanoma cells (Fig. 4b). Across six cells, the NRAS organization peaked at mid-range energy levels ($L = 13$ with a FWHM of 17 levels) corresponding to spatial scales of 7 µm (Supplementary Fig. 8d). NRAS is recruited to the membrane by bleb-related scaffold proteins[39]. We therefore hypothesized that the spatial scale of NRAS signaling relates to the length scale of bleb-induced surface undulations. We detected blebs on the cell surface using the u-shape3D software[34] (Supplementary Fig. 9). Compared with the bleb spectra, the NRAS spectra were somewhat skewed to lower frequency levels (Fig. 4bii,biii and Supplementary Fig. 9). We therefore concluded that although the bleb distribution in these melanoma lacks an axis of preferential organization, the NRAS distribution is at least in part determined by secondary, long-range mechanisms that structure organization at scales larger than that of blebs.

To check whether our framework could evaluate the spatial signature of a surface signal in a shape-invariant manner for an experimentally derived surface pattern, we transferred both a polka dot pattern and experimentally measured NRAS patterns from one cell to another cell using an orbifold Tutte embedding texture mapper[42].

The energy spectra of the original and mapped polka dot patterns and NRAS organization display similar spatial signatures on both cell surfaces (Supplementary Fig. 10a,b, top row). The spatial scales for five of the cells were preserved regardless of cell morphology (Fig. 4c and Supplementary Fig. 10b).

To further validate our framework, we measured the spatial organization across a perturbation with expected effects on the organization of septin. Septin is a curvature-sensitive molecule that associates to the base of blebs[39]. Bleb formation is inhibited by wheat-germ agglutinin (WGA)[43]. Thus, in untreated cells, septin is organized in patches near the base of blebs (Fig. 5ai, left), whereas the patches disappear under WGA treatment (Fig. 5ai, right), yielding a spectrum without a preferential scale. We measured the energy spectra of ten untreated cells and seven WGA-treated cells (Fig. 5aii). As per the Kolmogorov–Smirnov test on the average curves, the energy spectra are statistically distinct between the two conditions (P-value = 0.016).

Polarized cell signaling is often accompanied by polarized cell morphology. Our framework allows the disentangling of morphology-driven from signaling-driven polarization. For example, PI3K activity is known to be polarized in migrating melanoma cells that themselves have polarized morphologies[37]. We measured PI3K activity via a fluorescent biosensor (GFP-AktPH) both before and after treatment with a PI3K inhibitor (PI3Kα inhibitor). This biosensor reports PI3K activity by localizing to PI3K effector products PIP$_2$ and PIP$_3$. Even when the effects of a polarized morphology were excluded by applying cellular harmonics as the base functions, the high energy at low frequency levels indicated substantial polarization of the PI3K activity. Upon PI3K inhibition, the energy spectra are overall reduced (Fig. 5b,c), indicating that the spatial organization of the PI3K signal is governed at least partly by the PI3K activation level. The area under the energy curve for 13 cells demonstrates the energy reduction after PI3K inhibition for individual cells (Fig. 5c, inset). Moreover, even on a relative scale the energy density at low frequencies is suppressed, showing that PI3K inhibition abrogates polarity in signaling (Fig. 5d and Supplementary Video 4). Calculating the median frequency level of energy density spectra (dashed lines in Fig. 5d) before and after treatment, we found the trend of PI3K inhibition raising the frequency level of the energy density distribution (Fig. 5e). Among the 13 cells analyzed, nine exhibited a shift towards higher frequencies, indicating that for the majority of cells, the signaling became less polarized. This observation is consistent with conclusions drawn previously[37]. We also computed the averaged difference between the curves before and after treatment over 13 cells (Fig. 5f). The biggest difference occurs at low frequency levels, confirming that PI3K inhibition abrogates primarily the polarity in signaling but less so the fine-grained organization (purple arrow in Fig. 5f).

Discussion

Elucidating the organization of molecular distributions and signaling activities on cell surfaces in 3D is confounded by the complexity of relating surface patterns to a reference that allows comparative analyses across cell populations with widely variable morphologies. Here we introduce cellular harmonics to disentangle the differences in surface signal organization from differences in cell morphology. We implemented the LBO on individual cell shapes to define a complete basis that spans spatial frequencies and is well adapted to the morphological structures of the cell surface. To parameterize a molecular cell surface pattern, we generated spectra that capture the spatial scale signatures of the pattern.

Past approaches to quantifying molecular cell surface patterns in the face of cell morphological variation relied on a few global features to represent cell shape or constrained cell shape on micropatterns[11–13]. Our work introduces a mathematical construction to characterize the signal organization in a functional space that captures the full range of natural scales relevant to the regulation of molecular processes.
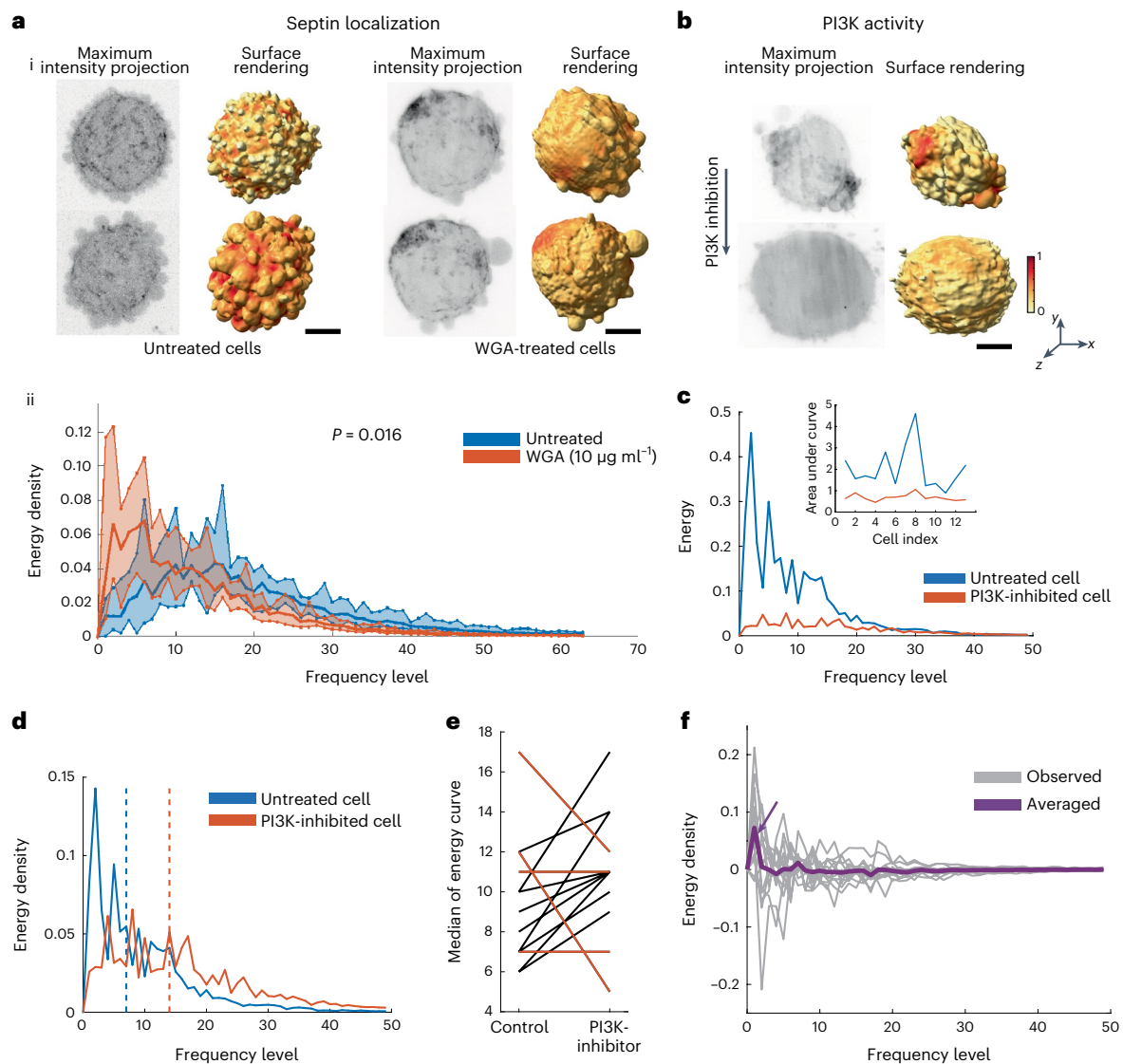
Fig. 5 | Evaluating the spatial redistribution of cell surface signaling on melanoma cells. ai, Maximum intensity projections and molecular surface projections of septin localization on untreated (left) and WGA-treated MV3 melanoma cells (right). **aii**, Energy spectra of septin organization in untreated cells (*n* = 10 cells) and WGA-treated cells (*n* = 7 cells). Bold curves indicate the mean of the energy density per level for each condition. Shaded bands indicate the range from the minimum to the maximum of the energy density per level for each condition. The *P*-value indicates two-sided Kolmogoroff–Smirnov test comparing the averaged energy curve in untreated and WGA-treated cells. **b**, Maximum intensity projections (left) and surface projections (right) of an MV3 melanoma cell, expressing GFP-AktPH, a marker of PI3K activity, before (top)

and after (bottom) PI3K inhibition. Scale bars, 2 μm **c**, Energy spectra of PI3K activity on the same cell before and after PI3K inhibition. Inset: area under the energy spectra curve of PI3K activity for 13 cells before and after PI3K inhibition. **d**, Energy density spectra of PI3K activity before and after PI3K inhibition. The dashed line indicates the median frequency level of the energy density spectra. **e**, Median energy density of PI3K activity between untreated and PI3K-inhibited cells (*n* = 13 cells). Cells exhibiting a non-positive shift after PI3K inhibition treatment, which deviates from the generally positive shifts, are indicated by red lines. **f**, The differences curve of energy spectra between untreated and PI3K-inhibited cells (gray curve is for a single cell, purple curve is averaged across 13 cells).

Our framework is thus suitable to experimental conditions, including in vivo imaging, that preclude external control over cell shape. The isometry invariant property of the LBO is often desired in shape matching, preserving the eigenvalue spectrum. Surfaces that change shape via folding without stretching are expected to be isometric across time, rending our framework particularly well-suited for evaluating molecular patterning on individual cells over time (Supplementary Videos 1 and 4). In general, the spectral decomposition of surface data enables the measurement and interpretation of the spatial organization of molecular distributions ranging from simulated data, such as signaling distributions on the cell surface, to larger scale phenomena, such as cytoskeletal distributions on embryo surfaces. The framework also provides a mathematically tractable yet complete representation

to power downstream analyses including generative modeling and machine learning.

The spatial scale of molecular organization is measured by the relative distances between aggregates; however, the spectra are non-informative of the aggregate sizes. This may be a limitation for certain biological applications. The accuracy of the spatial scales depends on the imaging resolution and measurement of marker signal intensity at the mesh surface. All image data presented in this work was Nyquist sampled (voxel side length of 160 nm with an isotropic optical resolution of generally 390 nm after deconvolution)[44]. Our default segmentation process generates a mesh surface with a number of nodes high enough to preserve the input imaging resolution. Using our framework, we can calculate the LBO for a mesh with ~100,000 nodes. However,

as shown in Supplementary Figs. 7 and 8a, the energy spectra of a molecular organization are robust in presence of spatial noise in the signal and down-sampling of the mesh. Thus, the proposed method is applicable to diverse image datasets, likely also of lower quality than those illustrated here.

The u-signal3D framework is made available as a collection of MATLAB functions bundled into a user-friendly interface. Underlying the implementation of u-signal3D is a robust computational pipeline for mesh triangulation and determination of LBO eigenvectors using algorithms that cope with both manifold and non-manifold cell geometries[24,35,36]. The LBO is critical to many computer graphics algorithms. The resources and validation provided by this work will aid the microscopy community in further adapting tools from the computer graphics field.

Methods

Cell culture and imaging

To validate our workflow, we used movie collections that were generated for past studies of various cellular processes. All cells were imaged via high-resolution light-sheet microscopy with isotropic resolution[40,44]. The cell preparation and imaging conditions for the CyOFP-tractin[40], NRAS-GFP[39], septin (SEPT6)-GFP[39] and PI3K activity (GFP-AktPH)[37] datasets are available in their respective papers. To simulate the polka dot patterns on observed cell geometries, we also used 67 cell surfaces from Driscoll and colleagues[34]. These cell surfaces included 27 MV3 melanoma cells expressing tractin-GFP, 29 dendritic cells expressing Lifeact-GFP, and 11 HBECs expressing tractin-GFP.

Cell surface generation

The pipeline embeds the cell surface generation modules from our previously published u-shape3D analysis framework[34]. Three-dimensional raw images of cells were deconvolved using either a Wiener filter with the Wiener parameter set to 0.018 (for CyOFP-tractin, NRAS-GFP and SEPT6-GFP localization) or a Richardson–Lucy algorithm (for PI3K activity). Images were apodized to reduce deconvolution artifacts, as previously described in ref. 40. The apodization height parameter set to 0.06 for all data except the PI3K dataset. We then smoothed the deconvolved images with a 3D Gaussian kernel (only for the PI3K dataset with $\sigma = 1.5$ pixels) and applied a gamma correction (0.7 for the PI3K and septin datasets, 0.6 for the NRAS dataset, and 1 for CyOFP-tractin). For the segmentation of melanoma cells in the PI3K, septin and NRAS datasets, we used the twoLevelSurface segmentation mode, which combines a blurred image of the cell interior with an automatically thresholded image of the cell surface. For melanoma cells labeled with CyOFP-tractin, cells were segmented at the intensity value specified by the Otsu threshold[45]. Finally, the triangle mesh representing the cell surface was smoothed using curvature flow smoothing[46].

Mesh characterization and validation

Triangle surface meshes generated from 3D microscopy images are prone to artifacts that adversely impact the LBO output. One such artifact is a multicomponent mesh, which often has isolated sets of disconnected triangles that do not correspond to the actual cell geometry (Supplementary Fig. 1a, black arrows) and can therefore be safely removed. Connected components of a mesh are identified by a list of mesh faces that share an edge. Smaller components are filtered out by a threshold defined on volume or surface area. For our data, we set the threshold to keep only the largest component of the cell surface. We used the 'remove_small_components' function from a public GitHub repository of the geometry processing toolbox (https://github.com/alecjacobson/gptoolbox).

For further processing, the cell surface must be represented as a closed two-manifold mesh satisfying two conditions: (1) each edge is incident to only two faces and (2) at each vertex of a face the face is embedded in a fan (Supplementary Fig. 1b). As some workflows may generate non-manifold meshes, as an option, we include a state-of-the-art LBO algorithm[24] that first creates a manifold mesh—termed a tufted mesh—from the non-manifold mesh before applying the LBO. In practice, we have not encountered a non-manifold mesh generated by our framework, thus we use the standard approach to compute the LBO, described below, by default.

Intensity measurement

We measured the fluorescence intensity local to each mesh vertex from the raw image. The background noise was first removed by subtracting the median pixel intensity outside the cell. Then, at each vertex, the average pixel intensity was computed within a sampling radius of 1 μm over the pixels inside the cell. Finally, we normalized each cell's surface intensity to a mean of one.

LBO calculation

The cell surface geometry is defined by vectors $\mathbf{X} = (x, y, z)$ of N triangle mesh vertices in a Cartesian coordinate system. The mesh vertices are connected in triangles to form mesh faces. To create a set of basis functions for a cell, we applied the LBO to the mesh. The LBO is a second-order differential operator defined as the divergence of the gradient of a function. On a triangle mesh, it computes the geometrical variation of the surface from a sphere. Mathematically, we aim to solve the following eigendecomposition equation to obtain the eigenvectors and eigenvalues of the LBO on a given mesh:

$$\Delta \phi_i = \lambda_i \phi_i. \tag{1}$$

Here ϕ_i denotes the i th eigenvector corresponding to the i th eigenvalue, λ_i, of the Laplacian Δ.

The Laplacian acting on an arbitrary discrete mesh has been extensively studied[15,23,35,36,46–49]. Most computational approaches are based on the co-tangent scheme[35,36], which is a form of first-order finite element method applied to the Laplacian on a surface. In the co-tangent formula (C), the LBO is an $N \times N$ symmetric matrix:

$$C_{ij} = \begin{cases} \frac{1}{2} \sum_{i \sim k} (\cot \alpha_{ik} + \cot \beta_{ik}) & \text{if } i = j \\ -\frac{1}{2} (\cot \alpha_{ij} + \cot \beta_{ij}) & \text{if } i \sim j \\ 0 & \text{otherwise} \end{cases} \tag{2}$$

where α_{ij}, β_{ij} are the two angles relative to edge ij as indicated in Supplementary Fig. 1bii. For the matrix element C_{ii}, the index k runs over all vertices connected to vertex i through an edge ik.

To obtain the LBO eigenvectors and eigenvalues, we used the function eigs() in MATLAB v.R2007 (MathWorks, Inc.) and later. The eigenvectors are frequency-based hierarchical functions that follow the protrusions of the 3D shape, respecting their symmetries. For example, for a sphere, the eigenvalues of the first frequency level ($L = 1$) are identical and correspond to three eigenvectors oriented in three orthogonal directions in 3D space. When the LBO is applied to an ellipsoid, where the symmetry is broken in one direction, the eigenvalue has higher magnitude in the short ellipsoid axis direction. Eigenvectors at the higher frequency levels follow the symmetry breaks of the ellipsoid to capture the shape variation relative to a sphere. In analogy, for a complex shape, the LBO eigenvectors follow the variation of the surface relative to a sphere (Fig. 2c).

Computation time depends on the number of LBO eigenvectors, which determines the frequency upper limit. Measuring the energy spectra up to $L = 50$ requires a few minutes. For raw images, additional time is needed for the cell segmentation process.

Representation of cell surface signals using LBO eigenvectors

Eigenvectors (ϕ_i) of the Laplacian constitute an orthogonal complete basis set. We can therefore extend a surface signal $u(\mathbf{X})$ in this basis,

$$u(\mathbf{X}) = \sum_i^N a_i \phi_i(\mathbf{X}) \tag{3}$$

where N is the number of Laplacian eigenvectors and a_i is the Laplacian eigenprojection of the ith eigenvector. The eigenprojections determine the contribution of each cell geometry defined eigenvector in parameterizing the signal $u(\mathbf{X})$. Based on the LBO eigenvectors and eigenprojections of a signal, the signal can be recreated ($\tilde{u}(\mathbf{X})$). To do so, we summed up the eigenprojections, multiplying each by the corresponding eigenvector to reconstruct the signal. To assess the reconstructed signal with its original values, we computed the absolute error ratio given by,

$$\text{Error} = \frac{\sum |u(\mathbf{X}) - \tilde{u}(\mathbf{X})|}{\sum u(\mathbf{X})}. \tag{4}$$

LBO frequency-level measurement

Application of the LBO (equation (1)) to a perfect sphere yields the spherical harmonics, $Y_{l,m}(\theta, \varphi)$, as shown in a frequency-level pyramid with the first levels shown in Fig. 2b. In spherical coordinates, the spherical harmonics are given by

$$Y_{l,m}(\theta, \varphi) \propto P_l^{|m|}(\cos\theta) e^{im\varphi} \tag{5}$$

in which, θ, φ define the colatitude and longitude, respectively; the indices l and m indicate the degree and order of the function in frequency-based levels; and $P_l^{|m|}(\cos\theta)$ represent the Legendre polynomials. The LBO encodes both the spatial angular frequency and its orientation over the eigenvectors.

Each frequency level has $2l + 1$ eigenvectors with similar spatial angular frequency. As an example, the second level ($l = 1$) of spherical harmonics has three identical eigenvectors corresponding to three harmonics, capturing three orthogonal spatial direction (Fig. 2b). Higher-level basis functions capture a greater number of pseudo-orientations with equal spatial scale. To quantify the spatial angular scale of a signal on a mesh surface, we collapsed the measurements from individual eigenvectors (frequency index) to a single value per level (frequency level), as we explain in the next section. Seeking to separate scale and pseudo-orientational information, we turned to a quantum mechanical interpretation of the spherical harmonics. The electron orbitals of an atom are simply described by the spherical harmonics pyramid shown in Fig. 2b, with each level of the pyramid corresponding to a distinct electron energy. Indeed, mathematically, all orbitals belonging to the same level have the same spatial angular frequency.

Although for complicated 3D shapes with lower symmetry compared to a sphere, eigenvectors at the same frequency levels have different eigenvalues, it is still reasonable to smooth the measurement over each level (l) to extract the spatial scale signature of a given molecular organization.

Dirichlet energy calculation

In computer geometry and shape analysis, the Dirichlet energy is often used as a metric of the smoothness of a function defined in a region[50]. The Dirichlet energy is given by

$$E = \frac{1}{2} \iint_\Omega \|\nabla w(\mathbf{X})\|^2 \, dA(\mathbf{X}) \tag{6}$$

where $w(\mathbf{X})$ is a function defined on the region Ω in three dimensions $\mathbf{X} = (x, y, z)$. Integration by parts yields,

$$\iint_\Omega \|\nabla w(\mathbf{X})\|^2 \, dA(\mathbf{X}) = \iint_\Omega w(\mathbf{X}) \Delta w(\mathbf{X}) \, dA(\mathbf{X}) \\ + \oint_\Omega w(\mathbf{X}) (\nabla w(\mathbf{X}) \cdot \mathbf{n}) \, dA(\mathbf{X}) \tag{7}$$

The first term on the right hand side is the Laplacian of the $w(\mathbf{X})$ in the region, and the second term, involving the scalar product between the Laplacian and normal vector ($\mathbf{n}$), relates to the boundary conditions. For a closed surface, such as a segmented cell, this term vanishes.

Substituting $u(\mathbf{X})$ for $w(\mathbf{X})$ subject to equation (1) and under consideration of the orthogonality of the LBO eigenvectors, the energy term equation (7) turns into,

$$
\begin{aligned}
E(u) &\sim \iint_\Omega u(\mathbf{X}) \Delta u(\mathbf{X}) \mathrm{d}A(\mathbf{X}) \\
&= \iint_\Omega \sum_{i,j}^N a_j^* a_i \lambda_i \phi_j^*(\mathbf{X}) \phi_i(\mathbf{X}) \mathrm{d}A(\mathbf{X}) \\
&= \iint_\Omega \sum_{i,j}^N a_j^* a_i \lambda_i \delta_{i,j}(\mathbf{X}) \mathrm{d}A(\mathbf{X}) \\
&= \sum_i^N a_i^* a_i \lambda_i
\end{aligned}
\tag{8}
$$

The Dirichlet energy in equation (8) is a scalar parameter. In our framework, the energy is computed per spatial angular frequency level to obtain an energy spectra. The energy per frequency level follows

$$e_l = \left\langle a_i^* a_i \lambda_i \right\rangle_{i=l_l}^{l_l + 2l + 1} \tag{9}$$

where l_l is the first index of the eigenvector at frequency level l. Similar to quantum physics, the $a_i^* a_i$ term gives the probability of the ith eigenvector contributing to the signal function $u(\mathbf{X})$, whereas λ_i is the eigenvalue corresponding to the eigenvector ϕ_i. As mentioned above, the eigenprojections per level indicate the dominant spatial scale of a given molecular organization without regard to shape symmetry variation. As fluorescence expression can vary from cell to cell, we normalized the energy spectra to 1 by dividing by the total energy (E in equation (8)) to define an energy density spectra for each cell that can be compared across a cell population.

Polka dot generation

We simulated polka dot patterns to validate the spatial scale of the measured signal distribution on a given mesh. As shown in Supplementary Fig. 3a, to generate uniform polka dot distributions, dot centers or seeds were first found by maximizing the minimum pairwise Euclidean distance amongst seeds. We used the 'farthest_point' function from a public GitHub repository of the geometry processing toolbox (https://github.com/alecjacobson/gptoolbox/external/toolbox_fast_marching). We then calculated the geodesic distance of all vertices from the closest seed using the fast marching method[51]. The polka dot pattern was then created by thresholding the surface over the list of geodesic distances, such that the fraction of total surface area occupied by polka dots was maintained across patterns. For the presented data, we found that 30% of the entire cell surface area has a higher energy peak magnitude for the polka dot surface area (Supplementary Fig. 3c). We set the edge mode parameter in the framework to 'sharp' for binary patterns and 'smooth' for gray patterns (Supplementary Fig. 3).

The generation of patchy polka dot patterns was similar to that of uniform polka dot patterns, except we kept only one-quarter of the pattern on one side of the cell surface. For non-uniform polka dot patterns, we randomly chose mesh vertices for dot centers and grew the seeds as mentioned above.

Noise generation

We generated two kinds of noise, intensity noise and spatial noise. In the first case, we added a random intensity value to each mesh node

drawn from a uniform distribution in the range of zero to a variable upper limit. We adjusted the noise level by changing the upper limit to a factor of the maximum intensity of either the polka dot pattern or the molecular organization. For the spatial noise, we translocated the mesh node values of painted area to a random node in a predefined neighborhood. The number of iteration for translocating each mesh node value was randomly selected from a Gaussian distribution with a standard deviation proportional to dot size. We controlled the noise level by changing the standard deviation of gaussian distribution.

Measuring the upper limit of the frequency level

The LBO is scale invariant. To measure the average distance between molecular aggregations on the cell surface, we painted the cell with various uniform polka dot distributions. The distance between dot centers was next calculated as the square root of surface area divided by the number of polka dots (Supplementary Fig. 8c). Depending on the cell surface, the energy peak levels vary with the number of polka dots, which corresponds to the distance between dots.

Texture mapping

We mapped the molecular (NRAS) organization from one melanoma cell surface to another using a texture mapping algorithm, Orbifold Tutte embeddings[42]. First, we chose four positional constraints on each mesh at top and bottom of the mesh by choosing from the minimum and maximum mesh node coordinates. We then used the 'Parallelogram' mode for finding the mapping matrix. Finally, we mapped a pattern from the mapped mesh to the primary mesh using the transpose of the mapping matrix.

Polka dot clustering

We constructed four polka dot patterns with 16, 64, 256 and 1,024 dots respectively on each of the 67 cell morphologies. For each pattern, we compiled a feature vector composed of the energy density spectra and then performed principal component analysis. The first three components contributed 58% of the total variance in the 77-dimensional feature space. To cluster the polka dot patterns, we employed the k-means algorithm in the 3D principal component space. The number of clusters was optimized to four using the silhouette distance. We calculated the mean of silhouette distances for each data point across each cluster, obtained by k-means clustering for cluster numbers ranging from 2 to 10.

Statistical analysis of drug inhibition

We used the two-sided Kolmogorov–Smirnov test to evaluate the septin energy spectra under WGA treatment. We calculated the P-value between the averaged energy spectra of untreated and treated cells.

To quantify the redistribution of PI3K activity after PI3K inhibition, we compared the energy spectra of individual cells before and after inhibition. We measured the median frequency level of each curve because the value of the energy spectra at higher frequencies is dominated by noise and thus the distribution is skewed relative to a normal distribution. We then computed the difference in the median before and after inhibition for 13 cells (Fig. 5e). Additionally, to evaluate the energy spectra over the entire frequency range, we averaged the difference curves between the before and after inhibition conditions for the 13 cells (Fig. 5f).

Visualization

Three-dimensional surface renderings of single cells were generated with ChimeraX v.1.2.5 (ref. 52) and some schematics were adapted from 'Cancer Cells' by BioRender.com (2022). ImageJ/Fiji (1.48v) was employed to prepare the MIP and slice images[53].

Reporting summary

Further information on research design is available in the Nature Portfolio Reporting Summary linked to this article.

Data availability

All image data that support the findings of this study are available in a Zenodo repository (https://doi.org/10.5281/zenodo.8166238)[54]. This repository comprises a collection of high-resolution 3D cell images captured using light-sheet microscopy. These images have been previously published, and the origin of the dataset is referenced in the Methods section. Source data for Figs. 2–5 are provided with this manuscript.

Code availability

All analysis was performed in a custom software package (u-signal3D) written in MATLAB (Mathworks), which is available as a frozen version in a Zenodo repository (https://doi.org/10.5281/zenodo.8222824)[55] and as an updated repository at (https://github.com/DanuserLab/u-signal3D).

References

1. Jordan, J. D., Landau, E. M. & Iyengar, R. Signaling networks: the origins of cellular multitasking. *Cell* **103**, 193–200 (2000).
2. Kholodenko, B. N. Cell-signalling dynamics in time and space. *Nat. Rev. Mol. Cell Biol.* **7**, 165–176 (2006).
3. Neves, S. R. et al. Cell shape and negative links in regulatory motifs together control spatial information flow in signaling networks. *Cell* **133**, 666–680 (2008).
4. Jaqaman, K. & Ditlev, J. A. Biomolecular condensates in membrane receptor signaling. *Curr. Opin. Cell Biol.* **69**, 48–54 (2021).
5. Edidin, M. Patches, posts and fences: proteins and plasma membrane domains. *Trends Cell Biol.* **2**, 376–380 (1992).
6. Schmick, M. & Bastiaens, P. I. H. The interdependence of membrane shape and cellular signal processing. *Cell* **156**, 1132–1138 (2014).
7. Driscoll, M. K. & Danuser, G. Quantifying modes of 3D cell migration. *Trends Cell Biol.* **25**, 749–759 (2015).
8. Elliott, H. et al. Myosin II controls cellular branching morphogenesis and migration in three dimensions by minimizing cell-surface curvature. *Nat. Cell Biol.* **17**, 137–147 (2015).
9. O'Shaughnessy, E. C. et al. Software for lattice light-sheet imaging of FRET biosensors, illustrated with a new Rap1 biosensor. *J. Cell Biol.* **218**, 3153–3160 (2019).
10. Peng, H. C. Bioimage informatics: a new area of engineering biology. *Bioinformatics* **24**, 1827–1836 (2008).
11. Schauer, K. et al. Probabilistic density maps to study global endomembrane organization. *Nat. Methods* **7**, 560–566 (2010).
12. Biot, E. et al. Strategy and software for the statistical spatial analysis of 3D intracellular distributions. *Plant J.* **87**, 230–242 (2016).
13. Pecot, T., Zengzhen, L., Boulanger, J., Salamero, J. & Kervrann, C. A quantitative approach for analyzing the spatio-temporal distribution of 3D intracellular events in fluorescence microscopy. *eLife* **7**, 32311 (2018).
14. Peng, T. & Murphy, R. F. Image-derived, three-dimensional generative models of cellular organization. *Cytometry A* **79**, 383–391 (2011).
15. Taubin, G. A signal processing approach to fair surface design. In *Proc. 22nd Annual Conference on Computer Graphics and Interactive Techniques* 351–358 (ACM, 1995).
16. Vallet, B. & Lévy, B. Spectral geometry processing with manifold harmonics. In *Comput Graph Forum* 251–260 (Wiley, 2008).
17. Reuter, M., Wolter, F.-E. & Peinecke, N. Laplace–Beltrami spectra as 'Shape-DNA' of surfaces and solids. *Comput. Aided Des.* **38**, 342–366 (2006).
18. Ducroz, C., Olivo-Marin, J. C. & Dufour, A. Characterization of cell shape and deformation in 3D using spherical harmonics. In *2012 9th IEEE International Symposium on Biomedical Imaging (ISBI)* 848–851 (IEEE, 2012).

19. Cammarasana, S. & Patane, G. Localised and shape-aware functions for spectral geometry processing and shape analysis: a survey & perspectives. *Comput. Graph. UK* **97**, 1–18 (2021).

20. Choukroun, Y., Shtern, A., Bronstein, A. & Kimmel, R. Hamiltonian operator for spectral shape. *Anal. IEEE Trans. Vis. Comput. Graph.* **26**, 1320–1331 (2020).

21. Melzi, S., Rodola, E., Castellani, U. & Bronstein, M. M. Localized manifold harmonics for spectral shape analysis. *Comput Graph. Forum* **37**, 20–34 (2018).

22. Neumann, T., Varanasi, K., Theobalt, C., Magnor, M. & Wacker, M. Compressed manifold modes for mesh processing. *Comput Graph. Forum* **33**, 35–44 (2014).

23. Belkin, M., Sun, J. & Wang, Y. S. Discrete Laplace operator on meshed surfaces. In *Proc. 24th Annual Symposium on Computational Geometry (SGG'08)* 278–287 (ACM, 2008).

24. Sharp, N. & Crane, K. A Laplacian for nonmanifold triangle meshes. *Comput Graph Forum* **39**, 69–80 (2020).

25. Petronetto, F., Paiva, A., Helou, E. S., Stewart, D. E. & Nonato, L. G. Mesh-free discrete Laplace–Beltrami operator. *Comput Graph Forum* **32**, 214–226 (2013).

26. Angenent, S., Haker, S., Tannenbaum, A. & Kikinis, R. On the Laplace–Beltrami operator and brain surface flattening. *IEEE Trans. Med. Imaging* **18**, 700–711 (1999).

27. Klein, A. et al. Mindboggling morphometry of human brains. *PLoS Comput. Biol.* **13**, e1005350 (2017).

28. Graichen, U. et al. SPHARA–a generalized spatial Fourier analysis for multi-sensor systems with non-uniformly arranged sensors: application to EEG. *PLoS ONE* **10**, e0121741 (2015).

29. Huang, S. G., Chung, M. K., Qiu, A. & Alzheimer's Disease Neuroimaging, I. Fast mesh data augmentation via Chebyshev polynomial of spectral filtering. *Neural Netw.* **143**, 198–208 (2021).

30. Qiu, A., Bitouk, D. & Miller, M. I. Smooth functional and structural maps on the neocortex via orthonormal bases of the Laplace–Beltrami operator. *IEEE Trans. Med. Imaging* **25**, 1296–1306 (2006).

31. Viana, M. P. et al. Integrated intracellular organization and its variations in human iPS cells. *Nature* **613**, 345–354 (2023).

32. Ruan, X. & Murphy, R. F. Evaluation of methods for generative modeling of cell and nuclear shape. *Bioinformatics* **35**, 2475–2485 (2019).

33. Shen, L., Farid, H. & McPeek, M. A. Modeling three-dimensional morphological structures using spherical harmonics. *Evolution* **63**, 1003–1016 (2009).

34. Driscoll, M. K. et al. Robust and automated detection of subcellular morphological motifs in 3D microscopy images. *Nat. Methods* **16**, 1037–1044 (2019).

35. Pinkall, U. & Polthier, K. Computing discrete minimal surfaces and their conjugates. *Exp. Math.* **2**, 15–36 (1993).

36. Ovsjanikov, M. et al. Computing and processing correspondences with functional maps In *SA '16: SIGGRAPH ASIA 2016 Courses* 1–60 (ACM, 2016).

37. Driscoll, M. K. et al. Proteolysis-free cell migration through crowded environments via mechanical worrying. Preprint at https://www.biorxiv.org/content/10.1101/2020.11.09.372912v3 (2022).

38. Ronchi, V. Forty years of history of a grating interferometer. *Appl. Opt.* **3**, 437–451 (1964).

39. Weems, A. D. et al. Blebs promote cell survival by assembling oncogenic signalling hubs. *Nature* **615**, 517–525 (2023).

40. Welf, E. S. et al. Quantitative multiscale cell imaging in controlled 3D microenvironments. *Dev. Cell* **36**, 462–475 (2016).

41. Charras, G. & Paluch, E. Blebs lead the way: how to migrate without lamellipodia. *Nat. Rev. Mol. Cell Biol.* **9**, 730–736 (2008).

42. Aigerman, N. & Lipman, Y. Orbifold tutte embeddings. *ACM Trans. Graph.* **34**, 190:191–190:112 (2015).

43. Charras, G. T., Coughlin, M., Mitchison, T. J. & Mahadevan, L. Life and times of a cellular bleb. *Biophys. J.* **94**, 1836–1853 (2008).

44. Dean, K. M., Roudot, P., Welf, E. S., Danuser, G. & Fiolka, R. Deconvolution-free subcellular imaging with axially swept light sheet microscopy. *Biophys. J.* **108**, 2807–2815 (2015).

45. Otsu, N. A threshold selection method from gray-level histograms. *IEEE Trans. Syst. Man Cybern.* **9**, 62–66 (1979).

46. Desbrun, M., Meyer, M., Schroder, P. & Barr, A. H. Implicit fairing of irregular meshes using diffusion and curvature flow. In *SIGGRAPH '99: Proc. 26th Annual Conference On Computer Graphics and Interactive Techniques* 317–324 (ACM, 1999).

47. Demanet, L. *Painless, Highly Accurate Discretizations of the Laplacian on a Smooth Manifold* Technical Report (Stanford University, 2006).

48. Mayer, U. F. Numerical solutions for the surface diffusion flow in three space dimensions. *Comput. Appl. Math.* **20**, 361–379 (2001).

49. Xu, G. Discrete Laplace–Beltrami operators and their convergence. *Comput. Aided Des.* **21**, 767–784 (2004).

50. Solomon, J., Guibas, L. & Butscher, A. Dirichlet energy for analysis and synthesis of soft maps. In *Comput Graph Forum* Vol. 32, 197–206 (Wiley, 2013).

51. Sethian, J. A. Fast marching methods. *SIAM Rev.* **41**, 199–235 (1999).

52. Goddard, T. D. et al. UCSF ChimeraX: meeting modern challenges in visualization and analysis. *Protein Sci.* **27**, 14–25 (2018).

53. Schneider, C. A., Rasband, W. S. & Eliceiri, K. W. NIH Image to ImageJ: 25 years of image analysis. *Nat. Meth.* **9**, 671–675 (2012).

54. Mazloom-Farsibaf, H., Zou, Q., Hsieh, R., Driscoll, M. K. & Danuser, G. *Data Repository Supporting "Cellular Harmonics for the Morphology-Invariant Analysis of Molecular Organization at the Cell Surface"* (Zenodo, 2023); https://doi.org/10.5281/zenodo.8166238

55. Zou, Q. *DanuserLab/u-signal3D* (Zenodo, 2023); https://doi.org/10.5281/zenodo.8222824

Acknowledgements

Author contributions

H.M-.F and M.K.D. conceived and designed the project. M.K.D. and G.D supervised the project. H.M.-F. wrote the codes for the package and M.K.D, Q.Z., and R.H. helped with writing and debugging the codes. H.M.-F. wrote the manuscript. M.K.D. and G.D helped with writing and editing the manuscript. All authors read and approved the final manuscript

Competing interests

The authors declare no competing interests.

Additional information

Supplementary information The online version contains supplementary material available at https://doi.org/10.1038/s43588-023-00512-4.

Correspondence and requests for materials should be addressed to Gaudenz Danuser or Meghan K. Driscoll.

Peer review information *Nature Computational Science* thanks Bruno Goud, Kristine Schauer and the other, anonymous, reviewer(s) for their contribution to the peer review of this work. Primary handling

editor Ananya Rastogi, in collaboration with the *Nature Computational Science* team.

Publisher's note Springer Nature remains neutral with regard to jurisdictional claims in published maps and institutional affiliations.

Corresponding author(s): Gaudenz Danuser

Last updated by author(s): Aug 30, 2023

Reporting Summary

Nature Portfolio wishes to improve the reproducibility of the work that we publish. This form provides structure for consistency and transparency in reporting. For further information on Nature Portfolio policies, see our Editorial Policies and the Editorial Policy Checklist.

Statistics

For all statistical analyses, confirm that the following items are present in the figure legend, table legend, main text, or Methods section.

n/a	Confirmed	
☐	☒	The exact sample size (*n*) for each experimental group/condition, given as a discrete number and unit of measurement
☐	☒	A statement on whether measurements were taken from distinct samples or whether the same sample was measured repeatedly
☐	☒	The statistical test(s) used AND whether they are one- or two-sided *Only common tests should be described solely by name; describe more complex techniques in the Methods section.*
☒	☐	A description of all covariates tested
☐	☒	A description of any assumptions or corrections, such as tests of normality and adjustment for multiple comparisons
☐	☒	A full description of the statistical parameters including central tendency (e.g. means) or other basic estimates (e.g. regression coefficient) AND variation (e.g. standard deviation) or associated estimates of uncertainty (e.g. confidence intervals)
☐	☒	For null hypothesis testing, the test statistic (e.g. *F*, *t*, *r*) with confidence intervals, effect sizes, degrees of freedom and *P* value noted *Give P values as exact values whenever suitable.*
☒	☐	For Bayesian analysis, information on the choice of priors and Markov chain Monte Carlo settings
☒	☐	For hierarchical and complex designs, identification of the appropriate level for tests and full reporting of outcomes
☒	☐	Estimates of effect sizes (e.g. Cohen's *d*, Pearson's *r*), indicating how they were calculated

Our web collection on statistics for biologists contains articles on many of the points above.

Software and code

Policy information about availability of computer code

Data collection	We used movie collections that were generated for previously published studies of various cellular processes. tractin-GFP38: Welf, E.S., Driscoll, M.K., Dean, K.M., Schäfer, C., Chu, J., Davidson, M.W., Lin, M.Z., Danuser, G. and Fiolka, R., 2016. Quantitative multiscale cell imaging in controlled 3D microenvironments. Developmental cell, 36(4), pp.462-475. NRAS-GFP37 and SEPT6-GFP : Weems, Andrew D., Erik S. Welf, Meghan K. Driscoll, Felix Y. Zhou, Hanieh Mazloom-Farsibaf, Bo-Jui Chang, Vasanth S. Murali et al. "Blebs promote cell survival by assembling oncogenic signalling hubs." Nature 615, no. 7952 (2023): 517-525. PI3K activity35 (GFP-AktPH): Driscoll, Meghan K., Erik S. Welf, Andrew Weems, Etai Sapoznik, Felix Zhou, Vasanth S. Murali, Juan Manuel Garcia-Arcos et al. "Proteolysis-free cell migration through crowded environments via mechanical worrying." bioRxiv (2022): 2020-11.
Data analysis	Software, which is available on https://github.com/DanuserLab/u-signal3D, was written in MATLAB. Multiple versions of MATLAB released in 2017a or later were used, but the software was specifically tested in MATLAB 2021a. 3D surface renderings of single cells were created by MATLAB and UCSF ChimeraX version 1.2.5 or later. Some schematics were created via Biorender.com (2022).

For manuscripts utilizing custom algorithms or software that are central to the research but not yet described in published literature, software must be made available to editors and reviewers. We strongly encourage code deposition in a community repository (e.g. GitHub). See the Nature Portfolio guidelines for submitting code & software for further information.

Data

> All data that support the findings of this study are available in a Zenodo repository (https://doi.org/10.5281/zenodo.8166238). The GitHub download contains two example dataset (https://github.com/DanuserLab/u-signal3D).

Human research participants

Reporting on sex and gender	n/a
Population characteristics	n/a
Recruitment	n/a
Ethics oversight	n/a

Note that full information on the approval of the study protocol must also be provided in the manuscript.

Field-specific reporting

Please select the one below that is the best fit for your research. If you are not sure, read the appropriate sections before making your selection.

☒ Life sciences   ☐ Behavioural & social sciences   ☐ Ecological, evolutionary & environmental sciences

For a reference copy of the document with all sections, see nature.com/documents/nr-reporting-summary-flat.pdf

Life sciences study design

All studies must disclose on these points even when the disclosure is negative.

Sample size	This package is a single-cell framework. No sample size was required for data analysis although we implemented the package for assessing the similarity of single-cell data across a cell population. In this case, sample sizes were chosen to be large enough for evaluation. For validation process, we used a wide range of various cell morphologies (67 cells), demonstrating the package is shape-invariant.
Data exclusions	Only isolated cells that were not in contact with other cells, were chosen. Cells with failed mesh surfaces were excluded.
Replication	We validated the software using synthetic data (polka dot patterns) and implemented it to three biological applications as described in the paper.
Randomization	Based on original papers for data collection, cells in high quality of cell health, marker expression, and optical clarity were imaged and analyzed.
Blinding	The software is robust and similar parameters of signal analysis were chosen for all cells in the same cell population. For cell segmentation, we optimized the parameters for each cell as mentioned in the Methods.

Reporting for specific materials, systems and methods

We require information from authors about some types of materials, experimental systems and methods used in many studies. Here, indicate whether each material, system or method listed is relevant to your study. If you are not sure if a list item applies to your research, read the appropriate section before selecting a response.

Materials & experimental systems

n/a	Involved in the study
☒	Antibodies
☒	Eukaryotic cell lines
☒	Palaeontology and archaeology
☒	Animals and other organisms
☒	Clinical data
☒	Dual use research of concern

Methods

n/a	Involved in the study
☒	ChIP-seq
☒	Flow cytometry
☒	MRI-based neuroimaging